ARCHITECTURE CIVIL ENGINEERING ENVIRONMENT
The Silesian University of Technology No. 1/2010

MODELLING OF CONCRETE BUILDINGS FOR PRACTICAL NONLINEAR SEISMIC RESPONSE ANALYSIS

Michael N. FARDIS*

*Prof.; University of Patras, Patras, Greece
E-mail address: *fardis@upatras.gr*

Received: 15.11.2009; Revised: 15.01.2010; Accepted: 17.02.2010

Abstract

Member modelling for the practical evaluation of the seismic performance of real concrete buildings on the basis of nonlinear dynamic analysis in 3D is overviewed. Fibre Element modelling is highlighted and contrasted to simplified lumped inelasticity models of members, with parameters fitted to a wealth of cyclic test results. An application to a full-scale 3-storey structure in 3D subjected to seismic testing under two horizontal components of ground motion validates this latter type of modelling. Two further applications are presented, one to explain the partial collapse of a multi-storey building in the Athens (1999) earthquake and another for the seismic assessment and retrofitting of a theatre building. The applications, which demonstrate simple lumped inelasticity member models, with parameters fitted to test results, are cost-effective and reliable alternatives to prohibitive Fibre Element modelling.

Streszczenie

W artykule przedstawiono modelowanie (na bazie nieliniowej analizy dynamicznej w 3D) elementów rzeczywistych budynków betonowych, służące do praktycznej oceny wpływu oddziaływań sejsmicznych. Wyróżniono modelowanie elementami pasmowymi, w odróżnieniu od uproszczonych niesprężystych modeli skupionych elementów z parametrami dopasowanymi do dużej ilości wyników badań cyklicznych. Wykonanie trójwymiarowego, naturalnej wielkości modelu 3-kondygnacyjnej konstrukcji poddanej obciążeniu sejsmicznemu, w postaci dwóch poziomych składowych ruchu gruntu, uzasadnia zastosowanie tego drugiego typu modelowania. Przedstawiono również dwa dalsze zastosowania, pierwsze do wyjaśnienia częściowego zawalenia się wielokondygnacyjnego budynku w wyniku trzęsienia ziemi w Atenach (1999) i drugie do oceny sejsmicznej i modernizacji budynku teatru. Przedstawione zastosowania dowodzą, że proste, niesprężyste modele skupione, z parametrami dostosowanymi do wyników badań są ekonomicznie efektywne i stanowią pewną alternatywę dla modelowania elementami pasmowymi.

Keywords: **Concrete buildings; Fibre models; Non-linear dynamic analysis; RC member models; Seismic response analysis; Seismic assessment.**

1. INTRODUCTION

Nonlinear dynamic seismic response analysis was developed in the 1970's, for research and code-calibration. Since then it has gained its place in seismic engineering practice for the evaluation of buildings designed conventionally (in force-based design with a global force reduction factor and linear analysis) or through cycles of analysis and design evaluation. The main practical application of nonlinear dynamic analysis, currently and in future, is for seismic assessment of existing structures. Professionals practicing seismic assessment and retrofitting are more specialised than those doing every-day seismic design and often master nonlinear dynamic analysis and its special software. A limitation of nonlinear dynamic analysis is a certain sensitivity of its outcome to the choice of input ground motions, which is at the absolute discretion of the engineer and often a source of doubt for the outcome of the analysis. Notwithstanding its current limita-

tions, nonlinear dynamic analysis is bound to become in the long run the technique of choice for practical seismic analysis.

For nonlinear static analysis under monotonically increasing non-seismic loads a concrete structure is often discretised at a point-by-point basis and modelled at the material level. A large number of Finite Elements (FEs) in 2D or 3D is used, with different Elements for the concrete and the reinforcing steel and possibly for bond. In principle such micro-models can reproduce even minor details in the geometry and follow the stresses and strains everywhere. However, computational and memory requirements restrict their use for seismic response analysis to individual members (e.g., a shear wall) or subassemblies (e.g. a beam and a column), preventing their application to full 3D structures. Practical nonlinear seismic response analysis of full RC structures is normally carried out with less sophisticated member-by-member models and one-to-one correspondence between elements in the model and members of the structure: using a single element for a beam, a column, the part of a wall between two floors, a panel of a floor-diaphragm between adjacent frames, etc. This allows sufficiently close representation of the key features of the behaviour and can describe the distribution of inelasticity and damage among and within members, with reasonable computational requirements even for large 3D structures. So, member-by-member modelling has been established as the main workhorse for practical nonlinear seismic response analysis of concrete structures and will remain so in the foreseeable future. Accordingly, only this modelling approach is covered here.

2. NONLINEAR MODELS FOR CONCRETE MEMBERS

2.1. Fibre models

The most general, fundamental and powerful model for one-dimensional members is the Fibre model. It is also best suited for inhomogeneous materials like RC. In a Fibre model the member is discretised longitudinally into segments, represented by discrete cross-sections, as well as at the cross-sectional level into finite regions. If bending is within a single plane (uniaxial), the section is discretised in strips or "fibres" normal to this plane. If bending is biaxial, the section is divided into a number of rectangular finite regions. A fibre comprises concrete and/or reinforcing steel, all lumped at its centroid. The nonlinear uniaxial σ-ε laws of the two materials are employed at that level. They can take into account stress reversals, concrete cracking, tension-stiffening and confinement, buckling of discrete bars, etc.

The normal strain at point (y, z) of the member section at x along its axis is related to the section deformation vector $\varepsilon_s(x) = [\varphi_y(x)\ \varphi_z(x)\ \varepsilon_o(x)]^T$ via the Bernoulli assumption: $\varepsilon(x, y, z) = B_s(y, z)\varepsilon_s(x)$, where $B_s(y, z) \equiv [z, -y, 1]$. The section force vector: $S_s(x) \equiv [M_y(x)\ M_z(x)\ N(x)]^T$ is derived from the normal stresses, $\sigma(y, z)$, over the section A as $S_s(x) = \int_A B_s^T \sigma(x, y, z) dA$ and incrementally related to ε_s as $dS_s(x) = K_s^t(x) d\varepsilon_s(x)$, where the section tangent stiffness matrix is:

$$\mathbf{K}_s^t(x) = \int_A E^t(x, y, z) B_s^T B_s dA \quad (1)$$

The tangent modulus $E^t(x, y, z) = d\sigma/d\varepsilon$ depends on the type of material at point (y, z) of section x and on its previous σ- and ε-history, through the material cyclic σ-ε law.

The element tangent stiffness matrix, $\mathbf{K}_m^t$, relates incrementally the nodal force vector at end nodes A and B, $S_m \equiv [M_y^A\ M_z^A\ M_y^B\ M_z^B\ N\ T]^T$, to the element deformation vector, $v_m \equiv [\theta_y^A\ \theta_z^A\ \theta_y^B\ \theta_z^B\ N\ T]^T$, where θ_y, θ_z are rotations at A and B with respect to chord AB ("chord rotations") and u, θ_T the relative displacement and twist of A and B along and about the x-axis: $dS_m = \mathbf{K}_m^t dv_m$. Early Fibre models adopted for the construction of $\mathbf{K}_m^t$ the "stiffness" approach, using an invariant interpolation function matrix $B_m(x)$ for element deformations: $d\varepsilon_s(x) = B_m(x)^T dv_m$. Then $\mathbf{K}_m^t$ is computed as $\mathbf{K}_m^t = \int_L \mathbf{B}_m(x)^T \mathbf{K}_s^t(x) \mathbf{B}_m(x) dx$ and the increment of the internal nodal force vector as: $dF_m = \int_L \mathbf{B}_m(x)^T d\mathbf{S}_s(x) dx$, where $d\mathbf{S}_s(x) = \mathbf{K}_s^t(x) d\varepsilon_s(x)$.

Integrations over x along the member length L are in general performed numerically, using equidistant integration stations for the trapezoidal rule, or at irregular intervals for more efficient schemes, such as Gauss or Gauss-Lobatto, with one integration station at each end and three to seven in-between. Serious problems may arise from this numerical integration: once inelasticity develops at member ends, the variation of $\varepsilon_s(x)$ with x deviates significantly from that imposed by an invariant $\mathbf{B}_m(x)$ matrix. As a matter of fact, invariance of $\mathbf{B}_m(x)$ during the response is against physical reality, because the distribution of inelasticity along the member changes after plastic hinging. Additional flexural deformations take place mainly in the vicinity of the yielding end(s) and

spread over the rest of the length with further loading. This may cause, e.g., spurious variation with x of the internal axial force $N(x) = \int_A \sigma(x, y, z)\mathrm{d}A$, which cannot be corrected by equilibrium iterations. A more serious problem arises when ultimate strength is reached at the end section(s). Then, if the end section continues loading on a post-ultimate-strength softening branch of the model, intermediate sections unload elastically. This behaviour cannot be reflected by an invariant $\mathbf{B}_m(x)$ matrix and causes numerical problems. Nonlinear analysis programs with "stiffness-based" fibre models sometimes attempt to by-pass the problem by using intermediate nodes between member ends, to capture the distribution of inelasticity along the member even with invariant $\mathbf{B}_m(x)$ between such nodes. To reduce computations, all Degrees of Freedom (DoFs) may be condensed out statically from these intermediate nodes, provided that they don't have lumped masses. Even when their DoFs are not condensed out, intermediate nodes do not increase very much the computational demands of the Fibre model, as these are controlled by the need to track fibre stresses and strains at the monitored sections and integrate numerically over these sections.

"Flexibility-based" Fibre models tackle some of the problems above. In them the section tangent flexibility matrix, $\mathbf{F}_s^t(x)$, obtained by inverting $\mathrm{K}_s^t(x)$, is integrated to give the element tangent flexibility matrix, $\mathbf{F}_m^t$:

$$\mathbf{F}_m^t = \int_A \mathbf{e}(x)^T \mathrm{F}_s^t(x)\mathbf{e}(x)\mathrm{d}x \qquad (2)$$

The element equilibrium matrix, $\mathbf{e}(x)$, relating $\boldsymbol{S}_s(x)$ to $\boldsymbol{S}_m$ as $\boldsymbol{S}_s(x) = \mathbf{e}(x)\boldsymbol{S}_m$, is exact no matter the distribution of inelasticity along the member, provided that there are no loads between its two ends. Note that $\mathrm{d}\varepsilon_s(x) = \mathbf{F}_s^t(x)\,\mathrm{d}\boldsymbol{S}_s(x) = \mathbf{F}_s^t(x)\,\mathbf{e}(x)\,\mathrm{d}\boldsymbol{S}_m = \mathbf{F}_s^t(x)\mathbf{e}(x)\mathrm{K}_m^t\mathrm{d}\boldsymbol{v}_m$, and therefore the incremental internal nodal forces, $\mathrm{d}F_m = \int_L \mathbf{B}_m(x)^T \mathrm{d}\boldsymbol{S}_s(x)\mathrm{d}x$, can be calculated on the basis of an non-invariant flexibility-dependent $\mathbf{B}_m(x)$ matrix, continuously updated during the analysis as $\mathbf{B}_m(x) = \mathbf{F}_s^t(x)\mathbf{e}(x)\mathrm{K}_m^t$ while the internal nonlinearities vary. An inconsistency between the section forces and the nodal forces persists regardless, this time between $\boldsymbol{S}_s(x) = \int_A \mathrm{B}_s^T \sigma(\mathrm{x}, \mathrm{y}, \mathrm{z})\mathrm{d}A$ and $\boldsymbol{S}_s(x) = \mathrm{e}(x)\boldsymbol{S}_m$. So do most numerical and physical problems of the "stiffness" approach. To solve them without intermediate nodes, more complex mixed two-field models have been proposed [1].

Fixed-end rotation at the end section of the member due to slippage of longitudinal bars from the joint region beyond that end may be taken into account by introducing a nonlinear rotational spring at that end, similar to those of the point-hinge model described in Section 2.2. The tangent flexibility of the nonlinear rotational springs which account for fixed-end rotations at end A or B within one of the two orthogonal planes of bending, xy or xz, is denoted here by f_A or f_B, respectively. These terms are added within each plane, xy or xz, to the diagonal ones, f_{AA} and f_{BB}, which relate the increments of inelastic chord rotations, $\mathrm{d}\theta_A$, $\mathrm{d}\theta_B$, with respect to chord AB to those of the end moments, $\mathrm{d}M_A$, $\mathrm{d}M_B$, in the Fibre model's element tangent flexibility matrix, $\mathbf{F}_m^t$:

$$\mathbf{F}_{m,total}^t = \begin{bmatrix} \cdot f_{AA} + f_A \cdot\cdot & \cdots\cdots f_{AB} \cdots\cdots \\ \cdots\cdots f_{AB} \cdots\cdots & \cdot\cdot f_{BB} + f_B \cdots \end{bmatrix} \qquad (3)$$

$\mathbf{F}_{m,total}^t$ is then inverted to give the tangent stiffness matrix of the element. At each end, let's say A, and within the corresponding plane of bending the tangent flexibility of the nonlinear fixed-end rotation spring may be approximated as $f_A = \theta_{y,slip}/M_y$ before flexural yielding and as $f_A = (\theta_{u,slip}-\theta_{y,slip})/(M_u-M_y)$ afterwards, where according to [2], [3], $\theta_{y,slip} = \varphi_y d_{bL} f_{yL}/(8\sqrt{f_c})$, $\theta_{u,slip} = 5.5 d_{bL}\varphi_u$ (f_y and f_c in MPa, d_{bL}: the diameter of longitudinal bars) and the yield and ultimate curvatures, φ_y, φ_u, and moments, M_y, M_u, are computed from the fibre discretisation of the end section or from first principles. The hysteresis loops of the springs for fixed-end rotation due to bond-slip are narrow, having inverted-S shape and should be simulated using cyclic models with pinching, as described in Section 2.4 and Table 2.

Fibre models can follow the spreading of inelasticity along the member, can reproduce pinching of moment-curvature (M-φ) hysteresis loops, account for coupling between the two directions of bending and with the axial direction and for varying axial load. They require, however, lengthy numerical operations at each step of the analysis and to keep track of the σ-ε history of each fibre and may be prone to instabilities. Tuning them to capture the experimental behaviour requires knowledge beyond that of design professionals. All things considered, it is not certain that the power and rationality of Fibre models warrant their generalised practical use.

2.2. "Point-hinge" or "lumped inelasticity" models with phenomenological M-θ relations, for uniaxial bending without axial-flexural coupling

In beams bending is uniaxial and axial-flexural coupling is commonly considered irrelevant. For walls, only inelastic flexure in their strong direction is of interest, while axial-flexural coupling, although important, is commonly ignored. In columns, the inelastic flexural response is often treated for simplicity independently in the two directions of bending and only few aspects of axial-flexural coupling are considered in each direction. So, uniaxial bending, with axial-flexural coupling ignored or treated in a simplified way, is of prime practical interest.

Under lateral actions flexural inelastic deformations are concentrated at and near member ends, since it is there that bending moments are maximum. So, in the most commonly used member models inelasticity is "lumped" at the ends of the member in zero-length "point hinges". The most common and useful "point hinge" model is the *one-component model*, comprising an elastic element with a nonlinear rotational spring in *series* at each end, where all inelastic deformations are lumped. The nonlinear end springs contribute to the tangent flexibility matrix of the member with diagonal terms f_A, f_B alone, as in Eq. (3). For uniaxial bending $\mathbf{F}_m{}^t$ is:

$$\mathbf{F}_m{}^t = \frac{L}{6EI}\begin{bmatrix} 2+a_A/p_A & -1 \\ -1 & 2+a_B/p_B \end{bmatrix} \quad (4)$$

– a_A is a zero-one variable for plastic hinging at end section A:

• $a_A = 0$, so long as M^A is less than the yield moment, M_y^A (before plastic hinging at A);

• $a_A = 1$ after plastic hinging there, i.e., for $M^A \geq M_y^A$;

– $p_A = (L/(6EI))/f_A$ is the current tangent stiffness of the rotational spring, as a fraction (hardening ratio) of the elastic stiffness of the member in skew-symmetric bending, $6EI/L$. During the course of cyclic loading or response, piece-wise constant values of f_A can be derived from the multi-linear primary loading-unloading-reloading rules given in Section 2.4.

Similarly for a_B and $p_B = (L/(6EI))/f_B$ at end B. Then the tangent stiffness matrix is:

$$\mathbf{K}_m{}^t = \frac{6EI/L}{3+2(a_A/p_A+a_B/p_B)+(a_A/p_A)(a_B/p_B)}\begin{bmatrix} 2+a_B/p_B & 1 \\ 1 & 2+a_A/p_A \end{bmatrix} \quad (5)$$

The section rigidity, EI, may be taken as the effective secant stiffness to the yield point, EI_{eff} , [2], [3]:

$$EI_{eff} = M_y L_s/(3\theta_y) \quad (6)$$

where L_s is the shear span (moment-to-shear-ratio) and M_y, θ_y are the moment and the chord rotation at yielding at the end section. Including in θ_y via the 3rd term the fixed-end rotation due to slip of bars from the joint region beyond the member end, we have with f_y, f_c in MPa [2], [3]:

• for beams or columns:

$$\theta_y = \varphi_y \frac{L_s + a_V z}{3} + 0.0014\left(1+1.5\frac{h}{L_s}\right) + \frac{\varphi_y d_{bL} f_y}{8\sqrt{f_c}} \quad (7a)$$

• for walls:

$$\theta_y = \varphi_y \frac{L_s + a_V z}{3} + 0.0013 + \frac{\varphi_y d_{bL} f_y}{8\sqrt{f_c}} \quad (7b)$$

where $a_V z$ in the 1st term is the tension shift of the moment diagram, with z the internal lever arm and with $a_V = 1$ if shear cracking precedes flexural yielding at the end section (i.e. if M_y/L_s exceeds the shear resistance without shear reinforcement, $V_{R,c}$); if $M_y < L_s V_{R,c}$ then $a_V = 0$.

If the member has different longitudinal reinforcement at its two end sections, Eq. (7) gives different values of EI_{eff} there. If the end sections are not symmetrically reinforced, EI_{eff} has different values for positive or negative bending. The EI values of members determine the natural periods and mode shapes of the elastic structure independently of the direction of loading; so, an average EI_{eff} for the two ends and directions of bending are used as EI in Eq. (5).

Different values of p_A and p_B in primary loading may be used at A and B (and for positive or negative bending for asymmetrically reinforced sections), but affect little the computed nonlinear seismic response. Default constant values, such as 0.05, 0.1, or even zero, are often used for them in primary loading. A more representative value may be estimated at each end from the member properties, including its ultimate chord rotation, θ_u, computed as in [2], [3]:

$$p = \frac{(M_u - M_y)/(\theta_u - \theta_y)}{M_y/\theta_y - (M_u - M_y)/(\theta_u - \theta_y)} \quad (8)$$

Unlike Fiber models, the point-hinge model cannot, in principle, account for coupling of the two directions of bending, and between them and the axial forces and deformations. When used for columns in 3D, it is often

in the form of independent uniaxial models in each one of the two orthogonal directions of bending. Although these two twin elements used for a column share its axial force and have 50% of its full axial stiffness each, the full value of the axial force should be used for the calculation of the properties of each one of the two elements. The values of EI and p_A, p_B for primary loading should be fixed during the response to the value due to the axial force for gravity loads alone. It is simple and normally does not create numerical problems to update the yield moment, M_y, and with it the hardening ratio for primary loading from Eq. (8), on the basis of the current axial force value. This will make a difference in the exterior columns of medium- or high-rise buildings and in the piers of coupled walls, where the axial force varies a lot during the seismic response. The value of M_y and the post-elastic primary loading branch derived from it via Eq. (8) may stay constant during further primary loading. After reversal, however, and while reloading in the opposite direction, the value of M_y in that direction should be updated according to the evolution of the axial force. By the same token, the value of the uniaxial yield moment signaling plastification of the end section may be taken to decrease due to a non-zero current moment component in the orthogonal direction. This is computationally cumbersome, not only because of the complications associated with biaxial moment interaction, but also because each one of the two independent uniaxial elements used for the column normally is unaware of the current state of bending in its companion.

An inflection point that stays steady after the member's first excursion into the inelastic range is a necessary condition for the inelastic part of the tangent flexibility matrix to be diagonal, (with diagonal terms f_A, f_B alone) without coupling between the two ends. A steady inflection point means fixed shear span, L_s, at each end section where plastic hinging may take place. Implicit in the calculation of EI_{eff} from Eqs. (6), (7) and of p_A, p_B from Eq. (8) is a constant value of L_s at each end. For frame members, it is natural to assume that plastic hinges develop in skew symmetric bending at both sections where the member frames into transverse ones within the plane of bending. Then, L_s is half the clear length from a beam-column joint to the next in the plane of bending: $L_s = L/2$. Plastic hinging in walls takes place only at the storey's bottom section and indeed with an imaginary point of inflection well above that storey. The shear span of the entire part of a wall between floors is the moment-to-shear ratio at the storey's bottom section; it is about 50% of the height from that section to the top of the wall.

2.3. The uniaxial moment-chord rotation (M-θ) curve in monotonic or primary loading

The monotonic M-θ curve is important, because hysteresis loops under cyclic loading are normally modelled using it as skeleton curve. Current force-based seismic design presumes that the global elastic stiffness of the structure corresponds to the elastic branch of a bilinear monotonic global force-deformation relation. This implies that the member monotonic M-θ curve is also bilinear, with elastic stiffness equal to the secant stiffness to yielding, Eq. (6).

The corner point of a bilinear M-θ relation in monotonic or primary loading is governed by the most critical (i.e. the weakest) mechanism of force transfer in the member: flexure, brittle shear or bond of longitudinal bars. If yielding of the end section takes place before brittle shear failure, the corner moment is the yield moment, M_y. Otherwise it is equal to $M = V_R L_s < M_y$, where V_R is the resistance in brittle shear and L_s is the shear span at the end in question.

A constant hardening ratio (post- to pre-yield stiffness) of the bilinear monotonic M-θ relation is given by Eq. (8). However, when the monotonic M-θ curve is taken as skeleton to the hysteresis loops in cyclic loading, a zero post-yield stiffness may be used, to make room for the post-elastic strength degradation typically induced by cyclic loading.

The end point of the monotonic or primary loading curve is the ultimate deformation. If it is governed by flexure, it equals to the ultimate chord rotation, θ_u, computed as in [2], [3]. A residual post-ultimate moment resistance may be retained in the model afterwards, but there is no solid technical support for the selection of its level. However, this is a purely academic question: for the performance of a structure to be verified as acceptable in practical applications, every single member, new, retrofitted, or existing and not retrofitted, should be verified in the end to have ultimate deformation well above the seismic demand. So, there is no real need to introduce an abrupt drop in resistance after the ultimate deformation.

Unlike the elastic stiffness, which should be the same, all other parameters of the monotonic or primary loading curve may be different for positive or negative loading, depending on how symmetric the geometry and the reinforcement of the section is.

2.4. Phenomenological models for the cyclic uniaxial M-θ behaviour

For cyclic loading the monotonic M-θ curve, serving as skeleton, is supplemented with hysteresis rules for post-elastic unloading-reloading cycles. The main objective of practical applications is the estimation of member peak seismic deformation demands, to be compared to the corresponding capacities. Peak demands are affected mainly by the energy dissipation inherent in the hysteresis rules and very little by the exact shape of the loops. An essential feature of the hysteresis model for application is its numerical robustness during any possible response history. Any numerical weakness of the model will certainly show up during at least one of the ground motions for which a system of possibly hundreds of members is analysed over thousands of time-steps with a few iterations per step. Numerical problems at the member level spread and develop into global ones. Even when the stabilising effect of inertia forces and damping salvages global stability, local numerical problems may lead to errors in member demands, which may remain unnoticed by an inexperienced eye. Simple and clear hysteresis models, with few rules describing the response under any cycle of unloading and reloading, are less prone to numerical problems than elaborate and presumptuous models, especially when complexity obscures certain possibilities with dangerous outcomes.

Multilinear unloading/reloading from/to the skeleton curve or a reloading branch is simple and efficient. If δ denotes deformation, unloading from a maximum ever value $\delta = \mu\delta_y$ on the primary loading branch is typically taken linear down to a residual value on the δ-axis, $\delta_{res} = \varepsilon\delta_y$, given in Table 1 for different models. If unloading to the δ-axis continues into first-time loading in the opposite direction, it heads linearly towards the yield point of the primary loading curve in that direction and follows its post-elastic branch thereafter. If the opposite direction has been revisited before, we have reloading. It is there that the model accounts or not for pinching of the hysteresis loop. If it doesn't, the extreme point ever reached on the primary loading curve in that direction normally becomes an effective yield point to which reloading linearly heads. Models without pinching [4]-[6] are more suitable for the M-φ than for the M-θ behaviour, as this includes the effects of shear and fixed-end rotation. For pinching [7]-[10] reloading heads first towards a corner point where the moment is $M_p = m_p M_y$ (m_p<1) and the deformation is $\delta_p = \mu_p\delta_y$. It then turns towards the extreme point ever reached on the primary loading curve in the current direction of reloading (see Table 2 for m_p and δ_p in different models with pinching).

Reloading after partial unloading (i.e., before the δ-axis is reached) follows the unloading path toward the point of last reversal. If unloading resumes before that point, it continues along the same unloading branch towards the δ-axis. If reloading turns into unloading before reaching the extreme past point on the primary loading curve in the current reloading direction, the unloading stiffness is the one corresponding to the original destination of reloading. In [7]-[10] reloading is directed to a point below (i.e. with lower peak resistance) than the extreme past point on the primary loading curve in the direction of reloading. However, strength decay with cycling has small effect on the computed response. For given primary loading curve, the response is more sensitive to the hysteretic energy dissipation addressed in Section 3.1.

Table 1.
Residual deformation after unloading from deformation $\delta = \mu\delta y$ on primary loading curve (μ> 1, p: hardening ratio of post-yield primary loading branch)

model	unloading rule	residual deformation $\delta_{res} = \varepsilon\delta_y$
[4]	unloading stiffness = elastic stiffness	$\varepsilon = (1-p)(\mu-1)$
[5] [7]	unloading stiffness = elastic stiffness times μ^{-a} ($a \approx 0.5$)	$\varepsilon = \mu - (1 + p(\mu-1))\mu^a$
[6]	residual deformation (1-α) times that in elastic unloading ($\alpha \approx 0.3$)	$\varepsilon = (1-\alpha)(1-p)(\mu-1)$
[8] [9]	extension of unloading goes to point on pre-cracking elastic branch in opposite direction where $M = aM_y$ ($a \approx 2$)	$\varepsilon = \dfrac{a(1-p)(\mu-1)}{a+1+p(\mu-1)}$
[10]		$\varepsilon = \dfrac{(1-p)(\mu-1)}{1+2p(\mu-1)}$

Table 2.
Moment and deformation at corner of bilinear reloading for models with pinching

model	reloading from (-) to (+) from residual deformation $-\varepsilon\delta_y^-$	m_p for $M_p = m_p M_y$; μ_p for $\delta_p = \mu_p \delta_y$
[8]	Reloading heads toward point where $M = \gamma M_y$ ($\gamma \approx 0.5$) on extreme past unloading branch in (+) direction from past peak deformation $\delta^+ = \mu_+ \delta_y^+$ on the primary loading branch to a residual one $\delta_{res}^+ = \varepsilon_+ \delta_y$; it stiffens toward δ^+ on the primary loading branch when δ_{res}^+ is reached	$m_p^+ = \frac{(\varepsilon_+ + \varepsilon_-)\gamma\left[1 + p_+(\mu_+ - 1)\right]}{(\varepsilon_+ + \varepsilon_-)\left[1 + p_+(\mu_+ - 1)\right] + \gamma(\mu_+ - \varepsilon_+)}$, $\mu_p^+ = \varepsilon_+$ interchange + and - for reloading from (+) to (-)
[9]	Reloading heads toward point on pre-cracking elastic branch in (+) direction where $M = \gamma M_y$ ($\gamma \approx 0.5$); stiffens toward peak past point on the primary loading branch when peak residual deformation $\delta_{res}^+ = \varepsilon_+ \delta_y$ is reached	$m_p^+ = \frac{(\varepsilon_+ + \varepsilon_-)\gamma}{\gamma + \varepsilon_-}$, $\mu_p^+ = \varepsilon_+$ interchange + and - for reloading from (+) to (-)
[10]	Reloading to a point on the elastic branch where $M = mM_y$ it stiffens then towards the peak past deformation on the primary loading branch	$m_p = m$, $\mu_p = m$ ($m = \min[1; 0.4L_s/h - 0.6] \geq 0$)
[7]	Reloading with stiffness m-times ($m < 1$) that of reloading to the peak past point on primary loading branch at $\delta^+ = \mu_+ \delta_y^+$; it heads to that point after reaching the M-axis	$m_p^+ = \frac{m\varepsilon_-\left[1 + p_+(\mu_+ - 1)\right]}{\mu_+ + \varepsilon_-}$, $\mu_p = 0$ interchange + and - for reloading from (+) to (-)

3. DAMPING

3.1. Hysteretic damping in cyclic uniaxial models

For post-yield cycles of given amplitude the hysteretic energy dissipation may be expressed as an effective hysteretic damping ratio, $\zeta = E_h/(4\pi F_{max}\delta_{max}/2)$, where E_h is the energy dissipated in a full cycle of loading-unloading-reloading with peak force F_{max} and deformation δ_{max}.

With ε according to Table 1, the first full cycle of loading-unloading-reloading to a peak ductility ratio $\pm\mu$ gives the following hysteretic damping ratio:

$$\zeta_{n=1} = \frac{2(\mu - 1)(1 - p + \varepsilon p) + 3\varepsilon}{4\pi\mu(1 + p(\mu - 1))} \tag{9}$$

Models without pinching and strength decay (e.g., [4], [5]) produce the following hysteretic damping ratio in a subsequent full cycle of unloading-reloading to a peak ductility ratio $\pm\mu$:

$$\zeta_{n>1,no-pinching} = \frac{\varepsilon}{\pi\mu} \tag{10}$$

except in [6], where reloading heads to a point on the primary loading curve at deformation $[\mu - \beta(\mu - 1)]\delta_y$, instead of $\mu\delta_y$. This gives:

$$\zeta_{n>1,[6]} = \frac{\varepsilon}{\pi\mu}\left(1 + \frac{\beta(1 - p - p\varepsilon)}{2(1 - \alpha)(1 + p(\mu - 1))}\right) \tag{11}$$

With m_p and μ_p from Table 2 and neglecting strength decay, models with pinching produce in a subsequent full unloading-reloading cycle to peak ductility ratio $\pm\mu$ a hysteretic damping ratio:

$$\zeta_{n>1,pinching} = \frac{1}{2\pi\mu}\left(\varepsilon - \mu_p + \frac{m_p(\varepsilon + \mu)}{1 + p(\mu - 1)}\right) \tag{12}$$

Data from cyclic tests on members suggest a damping ratio of about 8% in post-cracking, pre-yield load cycles, almost regardless of the amplitude of loading and of specimen characteristics. Fitting of the damping given by Eqs. (9)-(11) for hardening ratio p=0.02 to test data gave [11]:

– exponent a for unloading in [5], [7]:

$$a = 0.84 - 0.09L_s/h \tag{13}$$

– coefficient α for unloading in [6]:

$$\alpha = 0.75 - 0.095L_s/h \tag{14}$$

– pinching parameter m in [10]:

$$m = 0.465 \tag{15}$$

3.2. Viscous damping

If the response is elastic, nonlinear and linear dynamic analysis should give identical results. Linear dynamic analysis should produce the peak response of a Single-Degree-of-Freedom system given by the

elastic response spectrum, normally associated with a 5% viscous damping ratio. For consistency, nonlinear dynamic analysis should also have 5% viscous damping for elastic response. As in a seismic design context the upper limit of the elastic regime is yielding of the members, the 5% viscous damping should encompass all sources of damping up to member yielding, notwithstanding the finding mentioned above that the damping ratio in post-cracking, pre-yield load cycles is about 8%.

For convenience of numerical integration, the damping matrix **C** is typically of the Rayleigh type: $\mathbf{C}=\alpha_o\mathbf{M}+\alpha_1\mathbf{K}$, giving viscous damping ratio ζ at a circular frequency ω equal to:

$$\zeta = \frac{1}{2}\left(\frac{\alpha_o}{\omega}+\alpha_1\omega\right) \tag{16}$$

To have values of ζ as close as possible to $\zeta_o=0.05$ in the predominant frequency range of the response, we may specify $\zeta=\zeta_o$ at circular frequencies ω_1 and ω_2 straddling that range, to get:

$$\zeta = \frac{\zeta_o}{\omega_1+\omega_2}\left(\frac{\omega_1\omega_2}{\omega}+\omega\right) \tag{17}$$

A good choice for ω_1 is the average of the circular frequencies of the two modes with the highest modal base shears in two nearly orthogonal horizontal directions (An eigenvalue calculation in the elastic structure should precede the nonlinear dynamic analysis anyway, for insight into the predominant features of the expected response). Then, ω_2 may be chosen two to three times ω_1, bracketing the range of the 1st and 2nd modes in both horizontal directions. The resulting viscous damping ratio is lower than $\zeta_o=0.05$ at frequencies between ω_1 and ω_2 and higher outside that range. The further away the values of ω_1 and ω_2, the larger is the dip in damping ratio between them, to a minimum value of $\zeta=2\zeta_o\sqrt{(\omega_1\omega_2)}/(\omega_1+\omega_2)$ at $\omega=\sqrt{(\omega_1\omega_2)}$. The closer together ω_1 and ω_2 are, the steeper the increase in damping at higher frequencies.

4. APPLICATIONS AND COMPARISON WITH MEASURED DYNAMIC RESPONSE IN 3D

A capability has been developed for modelling and seismic response analysis of RC buildings and for their seismic assessment and retrofit design according to [3]. It has been incorporated in computer program ANSRuop [12], developed at the University of Patras as a significantly improved and expanded version of the ANSR-I program [13]. All types of seismic response analysis in [3] are covered, always in 3D. The modelling approach may be considered as the simplest one allowed in [3], yet representing fairly well the inelastic behaviour of members and of the structure as a whole. Key points of the modelling adopted are:

1. Point hinge models are used for all members according to Sections 2.2-2.4 above, with hysteresis rules as in [6], unloading parameter $\alpha = 0.3$ (see Table 1) and reloading parameter $\beta = 0$.
2. The element elastic stiffness is the secant to yielding, $(EI)_{\text{eff}}$, from Eqs. (6), (7), calculated with shear span according to the last paragraph of Section 2.2. The effective flange width of T- or L-beams on either side of the beam web is taken as 25% of the beam shear span or of the distance to the adjacent parallel beam (whichever is shorter); slab bars within this width which are parallel to the beam count into the top reinforcement of its end section(s).
3. Vertical members are modelled with independent elements in each bending plane, according to the paragraph after Eq. (8). Twin elements modelling walls with non-rectangular section are located at the shear centre of the section. The yield properties of the column or wall twin elements evolve with the value of the axial load.
4. Joints are rigid; slip of the reinforcement of members framing in the joint from or through it affects the member effective stiffness (see the 3rd term in Eqs. (7)), as well as the ultimate chord rotation.
5. Eccentricities in the connections between members are modelled by rigid elements.
6. The in-plane flexibility of individual panels of floor diaphragms is considered, by taking the beams at the boundary of a panel (including balconies) as prismatic elements in 3D with moment of inertia about an axis normal to the floor plane and cross-sectional area such that the extensional and shear stiffness of the floor panel is approximated.
7. Staircases are included in the model. Landings between floors, as well as their supporting beams, are modelled according to point 6 above. Straight flights are modelled according to points 1 to 5 as oblique columns (i.e. with two independent elements having strength and stiffness in both trans-

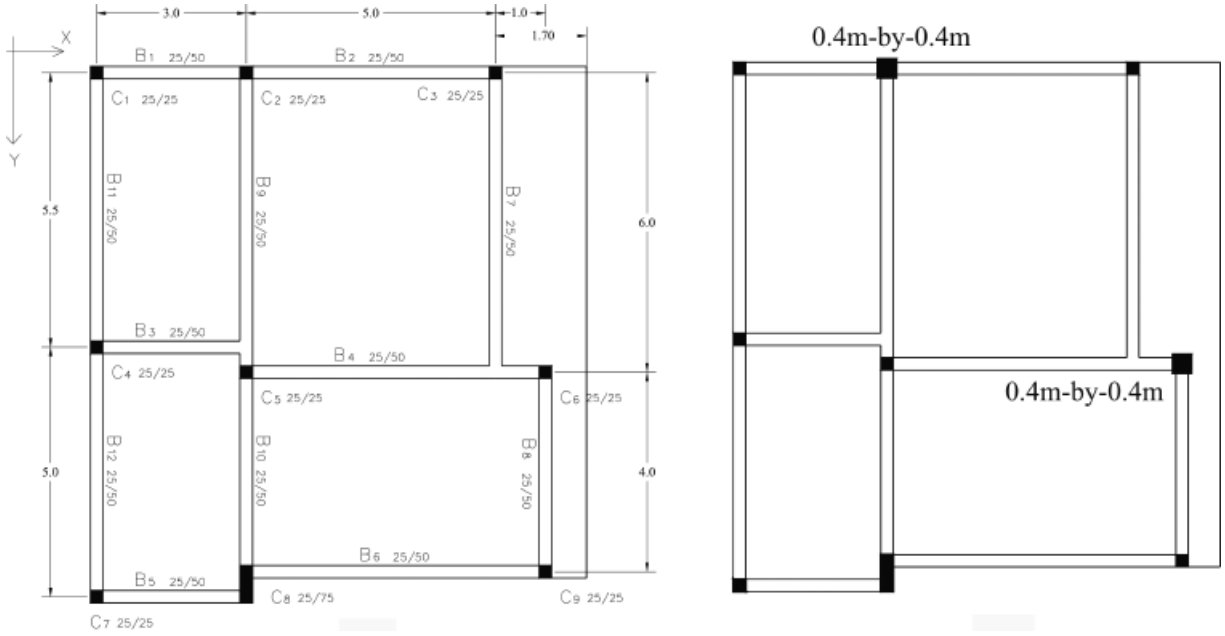

Figure 1.
SPEAR frame: (left) un- or FRP-retrofitted, (right) with columns C2, C6 RC-jacketed

Figure 2.
SPEAR test structure frame: (left) un-retrofitted, (right) retrofitted with FRP jackets

verse directions) between the two nodes belonging to vertical elements which are closest to the axis of the flight at the two horizontal levels it connects.

8. A damage index is calculated at each member end. It is taken as the ratio of the demand from the analysis to the corresponding capacity, as both evolve during the response. For vertical members demand-capacity-ratios in the two orthogonal planes of bending are combined via the SRSS rule into a single damage index. The peak value of the damage index during the response is reported in the end. Values near 1.0 signify likely or incipient failure. Flexural damage is evaluated in terms of chord rotations, using as capacity the empirical ultimate chord rotation according to [2], [3], with modifications due to lack of detailing for earthquake resistance, lap-splicing of vertical bars, FRP-wrapping, etc. Shear damage is evaluated in terms of shear forces, with capacities for failure by diagonal tension after yielding or by diagonal compression before or after yielding, according to [14], [3].
9. P-Δ effects are included.

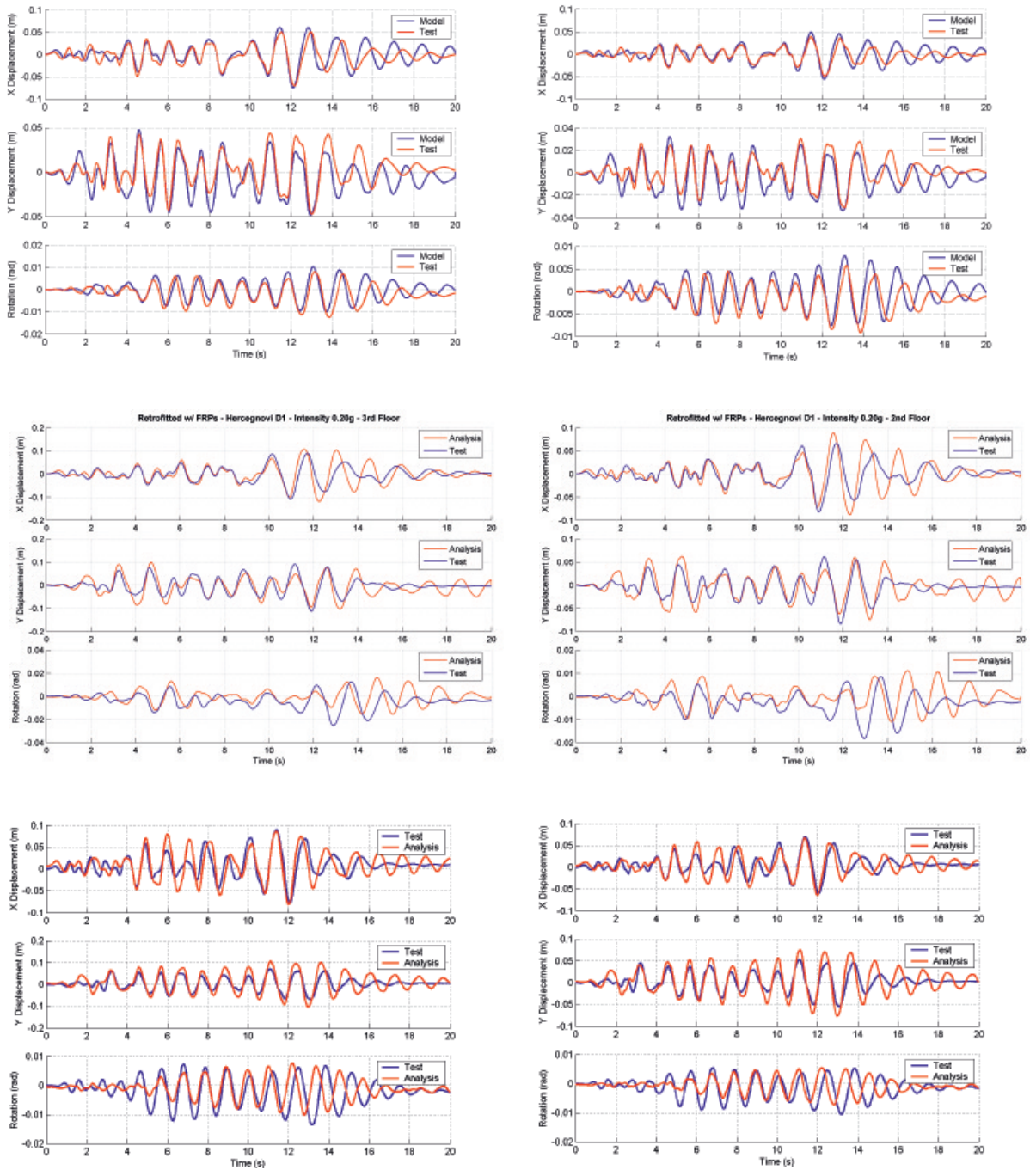

Figure 3.
Translation and twist time-histories of 3rd (left) and 2nd (right) floor - Analysis v test of SPEAR frame: (top) unretrofitted; (middle) for FRP-wrapping; (bottom) with RC jackets [17]

10. Masses are lumped at the nearest node of the model.
11. Rayleigh damping is used, with 5% damping specified according to the last paragraph of Sect. 3.2.

Modelling and analysis capability is applied to the 3-storey full-scale building of Figs. 1 and 2, designed within the SPEAR project according to practice of the 1950s in Greece [15]. It was subjected to bi-directional PsD testing at ELSA [16] in three versions:

- unretrofitted (Figs. 1 (left) and 2 (left));

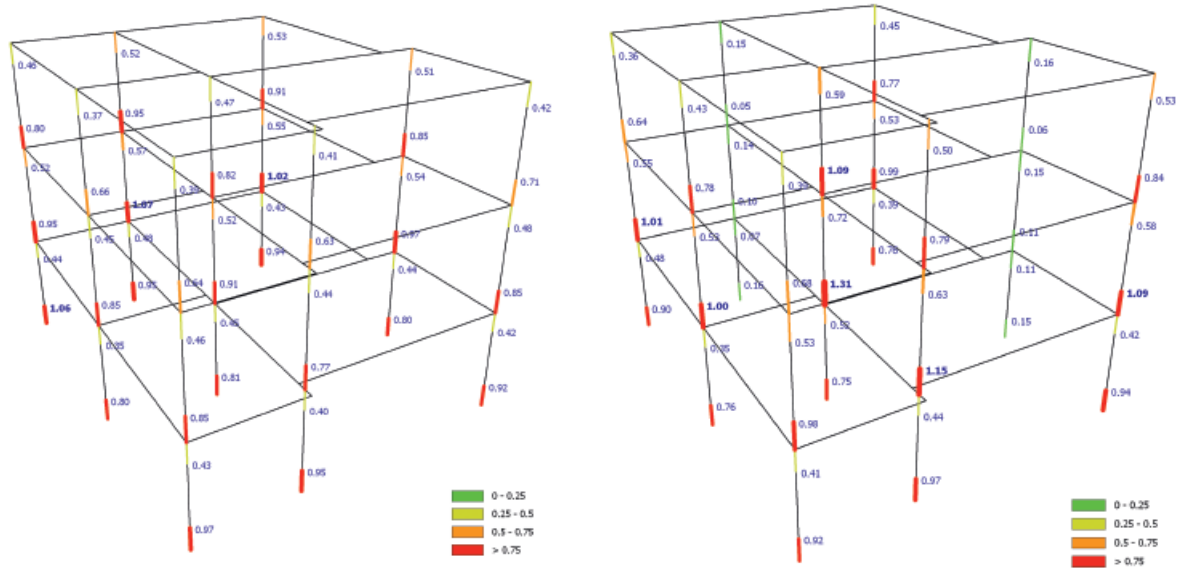

Figure 4.
Column demand-capacity ratio ("damage index") in flexure of SPEAR structure: (left) unretrofitted at a PGA of 0.15g; (right) with two columns RC jacketed at PGA of 0.2g [17]

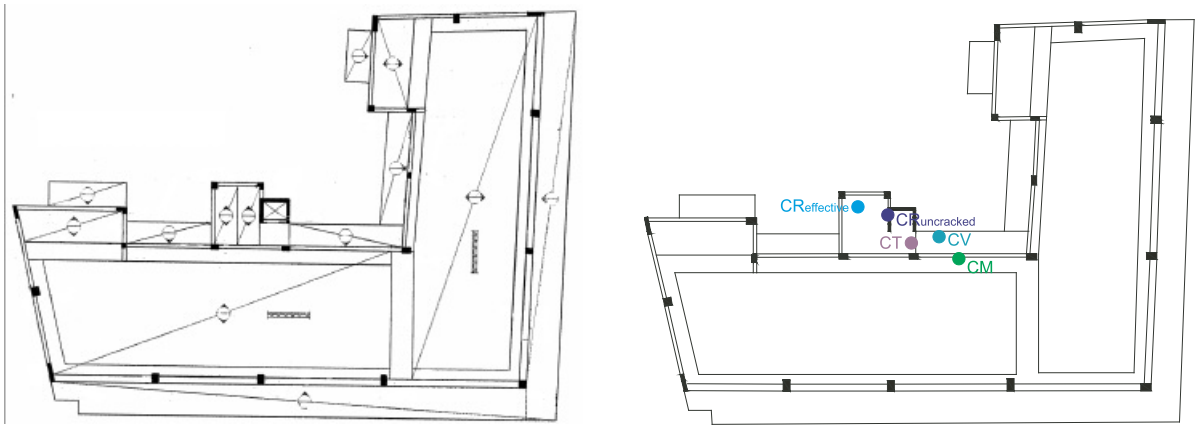

Figure 5.
Building that collapsed during the Athens (1999) earthquake: (left) standard storey; (right) centres of mass, stiffness or resistance and pole of twist at 1st floor

- retrofitted with Fibre-Reinforced Polymers (FRPs) as follows (Figs. 1 (left) and 2 (right)):

– the ends of all 0.25 m columns in all storeys were wrapped with two layers of uni-directional Glass FRP (GFRP) over 0.6 m from the face of the joint, for confinement;

– bi-directional GFRP was applied in two layers for shear strengthening: (a) at exterior faces of corner joints, and (b) all around and along column C8 (also for confinement).

with the central columns of the two "flexible" sides concrete-jacketed from 0.25 m to 0.4 m square after removal of the FRPs, to mitigate the torsional imbalance (Fig. 1 (right)).

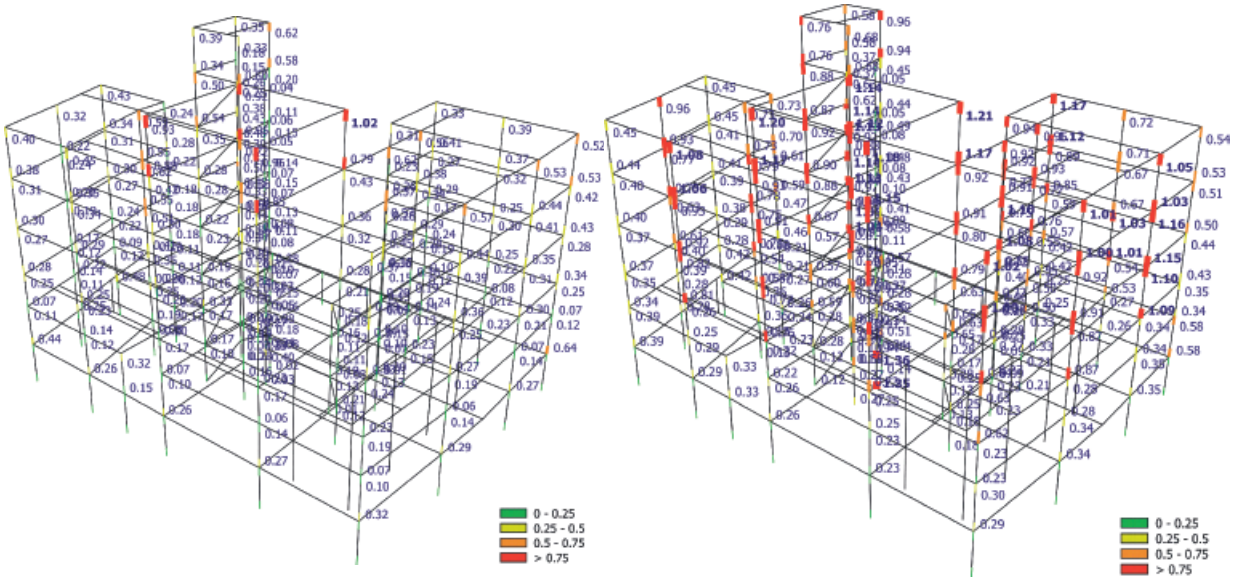

Figure 6.
Mean value of column damage indices in flexure (left) or shear (right) from analyses for the 30 most likely bidirectional ground motions at the site in the Athens 1999 earthquake

Pre-test nonlinear response-history simulations were carried out [17] for the following PsD tests, which used as bidirectional motion the two Herzegnovi records of the Montenegro 1979 earthquake, modified to simulate EC8-spectra-compatible ground motions for soil type C:

– Unretrofitted frame; peak ground acceleration (PGA) in both directions 0.15 g, Fig. 3, top.
– FRP-retrofitted structure; bidirectional motion scaled to a PGA of 0.2 g, Fig. 3, middle;
– Frame with columns C2, C6 jacketed; same motions scaled to a 0.2 g PGA, Fig. 3, bottom.

To emulate the very tight fixing of the building's stiff and strong foundation to the laboratory strong floor, all columns are considered fixed at their connection to the foundation.

Fig. 3 compares the predicted floor translation and twist time-histories to those measured [17]. Overall agreement is good, confirming the modelling assumptions above. The flexural damage indexes computed by the end of the dynamic response are shown in Fig. 4 for two of the PsD tests. The pattern of damage in Fig. 4 is consistent with the observed one: in the unretrofitted structure flexural damage was indeed significant at most column ends; at the 2nd storey and on the "flexible" sides of the building plan flexural damage was serious; the 0.20g-PGA motions inflicted no visible damage to the FRP-retrofitted structure, consistent with predicted damage index values less than 0.5. In the frame with the two RC-jacketed columns on the "flexible" sides, the central column failed in flexure at the 2nd storey – as predicted in Fig. 4 – as well as at the 1st storey. Consistent with the predicted shear damage indexes, there were no indications of shear effects in the damaged or failed regions of members. This validates the expressions in [2], [3], [14] for the flexure-controlled ultimate cyclic chord rotation and the degradation of shear resistance with cyclic loading, respectively.

Following its validation on the basis of the PsD test results, the same modelling and type of analysis are applied to two real RC buildings with little engineered earthquake resistance and various types of irregularity in plan and elevation. First, to the 5-storey (plus penthouse and basement) building in Fig. 5. The wing of the L-shaped plan to the right of the elevator shaft and of the column across the slab collapsed in the Athens 1999 earthquake. To identify the collapse mechanism, a series of nonlinear response-history analyses have been carried out under six ground motions derived as "most likely" at the site on the basis of several ground motion records in the Athens area and of the detailed subsoil conditions at the recording stations and at the building site [15]: each of the six motions is applied once in one horizontal direction and any other at at right angles,

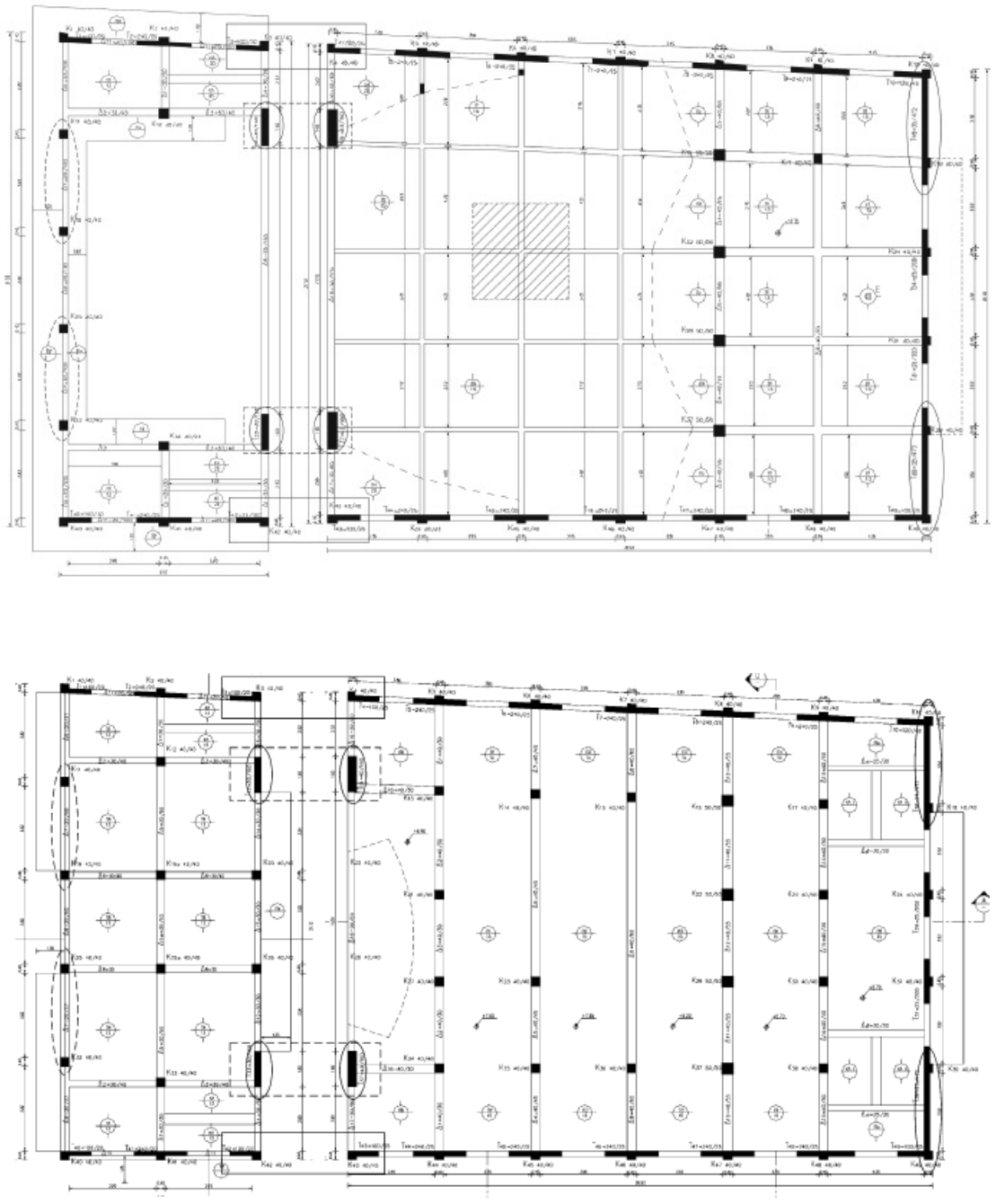

Figure 7.
Plan of theatre facility. Top: roof; bottom: ground floor. Left: Stage; right: Theatre

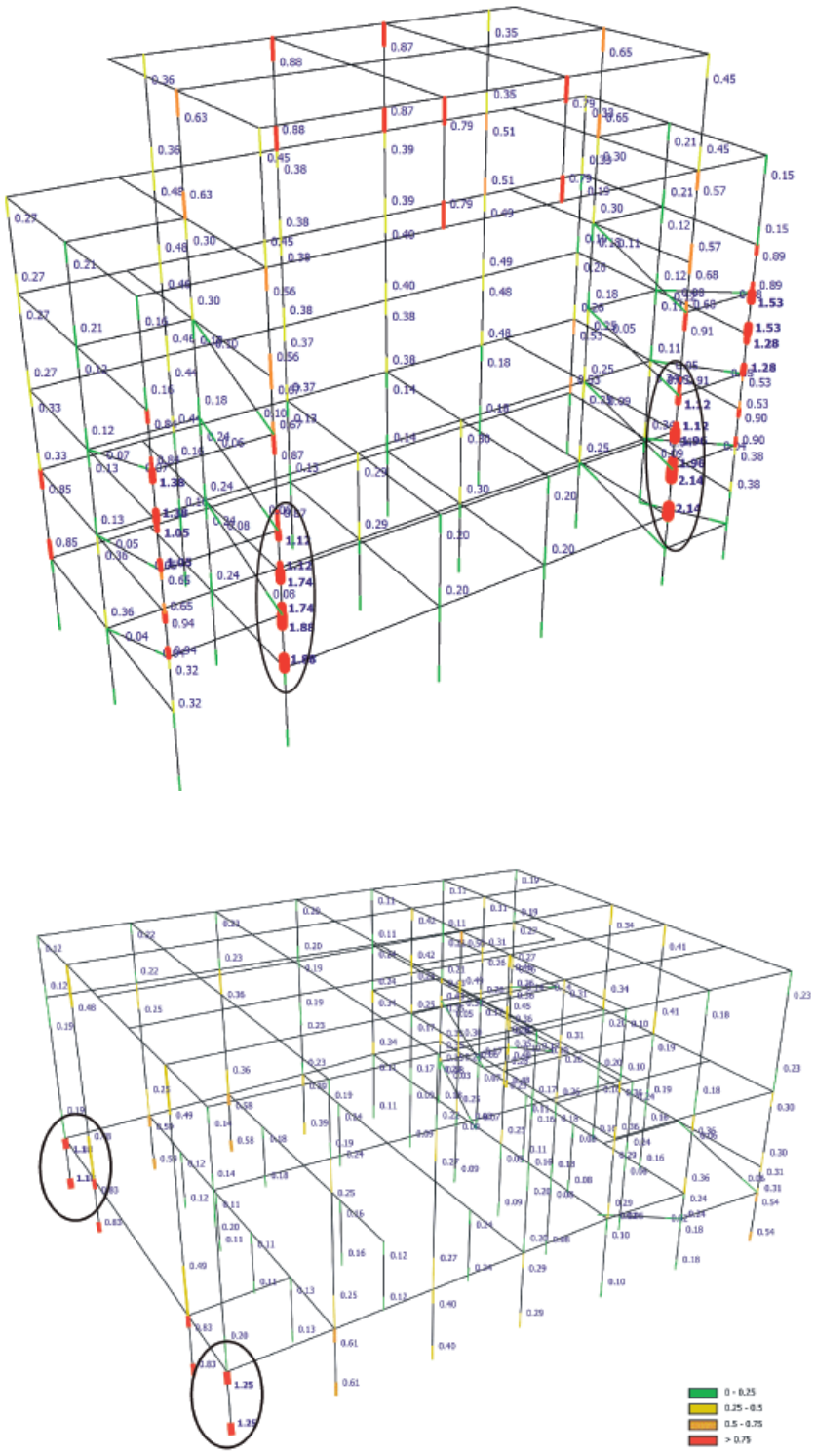

Figure 8.
Shear force damage index in vertical members of Stage (up) and Theatre (bottom) of as-built theatre facility (mean value over 56 bidirectional ground motions at PGA 0.1 g)

giving 30 bidirectional motions in total. All vertical members are considered fixed at the top of the basement within the plane of the stiff, storey-high wall at the basement's perimeter, being integral with that wall.

The response time-histories for the individual bidirectional motions and the natural periods and modes show that higher modes controlled the response. Owing to the flexible connection of the floors to the stiff elevator shaft and to the staircase next to it, higher mode response generally entails out-of-phase twisting of the shaft/staircase relative to the rest. The damage indices in Fig. 6 (left) show in red the penthouse columns as near-critical in biaxial bending. Fig. 6 (right) shows also that these columns, as well as at least five others in the upper storeys of the right-hand wing, are all critical in shear. This suggests that collapse started with shear failures of columns at the penthouse and in the upper storeys of the part of the building to the right of the elevator shaft. Floor diaphragms, being almost unreinforced in their secondary direction, were unable to transfer forces from the deficient right-hand-side to the stronger wing on the left and teared along a line next to the shaft to the opposite side in plan.

The 2nd application is to a theatre facility of the early 1970's on the island of Kephalonia (GR). The design was to codes of the 1950s for a PGA of about 0.1 g without detailing for ductility. Current codes specify a PGA of 0.36 g even for ordinary buildings. Reinforcement corrosion at all exterior elements triggered seismic assessment and retrofitting, as the first-in-history application of Eurocode 8, Part 3 [3]. Nonlinear dynamic analyses have been carried out for 56 semi-artificial bidirectional ground motions. Each motion emulates the two components, X and Y, of seven historic earthquakes, each component modified to fit the Eurocode 8 elastic spectrum for 5% damping and soil C. As the framing plan is asymmetric, each component is applied in the positive or negative X or Y sense, giving $7x2^3 = 56$ motions. The building (including the foundation) is in two independent parts (Fig. 7). Vertical members are considered fixed at the top of deep two-way foundation beams for the Theatre part, or of a basement-deep perimeter wall plus heavy two-way foundation beams under the Stage part. Pounding of the two parts of the building across the joint is neglected in the dynamic analysis.

The damage indices in shear in Fig. 8 show that a seismic action with 0.1 g PGA causes shear failure of the two pairs of walls next to the joint: the two interior ones parallel to the joint at the Stage, the two exterior ones at right angles to the joint in the Theatre part. Twisting of each part about a vertical axis closer to the side(s) opposite to the joint is a factor for these failures [18]. To eliminate this factor the two parts of the building were connected across the joint, at the two sides of the building and the roof. To counter reinforcement corrosion and upgrade the structure to a design PGA of 0.36 g, heavily reinforced concrete overlays were added to the exterior face of vertical elements all along the sides, except at the façade on the right in Fig. 7 [18]. A certain shear deficiency in the two large walls of that façade was corrected via externally bonded Carbon FRPs (CFRPs). To balance these two walls, two large RC walls were added at the façade on the left in Fig. 7. Finally, a shear deficiency in the two pairs of interior walls along the joint was also corrected with CFRPs bonded to their accessible sides. All these retrofitting measures have been governed by the difficulty to connect new elements to the foundation anywhere except at the exterior of three sides of the building. Nonlinear dynamic analyses for the same suite of 56 bidirectional motions, this time scaled to a PGA of 0.36 g, show that the retrofitted building is acceptable according to [3].

5. CONCLUSIONS

Nonlinear dynamic analyses in 3D of real concrete buildings for practical seismic performance evaluation or upgrading according to [3] can use simplified lumped inelasticity member models, with properties and parameters fitted to a wealth of cyclic test results. The power and rationality of Fibre models can best be used in the realm of research, provided that the skills and experience necessary to master their tricky numerical performance are available.

REFERENCES

[1] *Taucer F., Spacone E., Filippou F.*; A Fiber Beam-Column Element for Seismic Response Analysis of Reinforced Concrete Structures. Earthquake Engineering Research Center, Rep. UCB/EERC 91-17, 1991, Univ. of California, Berkeley, Ca.

[2] *Biskinis D., Fardis M.N.*; Cyclic Strength and Deformation Capacity of RC Members, Including Members Retrofitted for Earthquake Resistance. Proceedings of 5th International fib PhD Symposium in Civil Engineering, Delft, 2004; p.1125-1133

[3] CEN European Standard EN 1998-3:2005. Eurocode 8: Design of Structures for Earthquake Resistance. Part 3: Assessment and Retrofitting of Buildings, Comite Europeen de Normalisation, 2005; Brussels

[4] *Clough R., Johnston S.*; Effect of Stiffness Degradation on Earthquake Ductility Requirements. Trans. Japan Earthq. Engineering Symposium, Tokyo, 1966; p.195-198

[5] *Anagnostopoulos S.*; Nonlinear Dynamic Response and Ductility Requirements of Building Structures Subjected to Earthquakes. Research Report. No. R72-54, 1974, Dept. of Civil Engineering, Massachusetts Institute of Technology, Cambridge, Ma.

[6] *Otani S.*; Inelastic Analysis of R/C Frame Structures. Journal of Structural Division, ASCE, Vol. 100, ST7, 1974; p.1433-1449

[7] *Coelho E., Carvalho E.C.*; Nonlinear Seismic Behaviour of Reinforced Concrete Structures. Proceedings of 9th European Conf. on Earthq. Engineering, 1990; Moscow

[8] *Park Y., Reinhorn A., Kunnath S.K.*; IDARC: Inelastic Damage Analysis of Reinforced Concrete Frame-Shear-Wall Structures. Technical Report NCEER-87-0008, 1987, Nat. Center for Earthq. Engineer. Research, State Un. of New York, Buffalo, N.Y.

[9] *Reinhorn A., Kunnath S., Panahshahi N.*; Modelling of RC Building Structures with Flexible Floor Diaphragms (IDARC 2). Techn. Rep. NCEER-88-0035, 1988, Nat. Center for Earthq. Engineer. Research, State Un. of New York, Buffalo, N.Y.

[10] *Roufaiel M., Meyer C.*; Analytical Modeling of Hysteretic Behavior of R/C Frames. ASCE, Journal of Structural Engineering, Vol.113 (ST3), 1987; p.429-444

[11] *Fardis M.N., Panagiotakos T.*; Hysteretic Damping of Reinforced Concrete Elements. Proceedings of 11th World Conf. on Earthq. Engineering, Acapulco, 1996

[12] *Kosmopoulos A., Fardis M.N.*; Seismic Evaluation of Strongly Irregular and Torsionally Unbalanced Concrete Buildings. Proceedings 2nd fib Congress 2006; Napoli

[13] *Mondkar D., Powel G.*; ANSR-I General Purpose Program for Analysis of Structural Response. Research Report UCB/EERC 75-37, 1975, Earthquake Engineering Research Center, Un. of California, Berkeley, Ca.

[14] *Biskinis D, Roupakias G., Fardis M.N.*; Degradation of Shear Strength of RC Members with Inelastic Cyclic Displacements. ACI Structural Journal, Vol.101, No.6, 2004; p.773-783

[15] *Kosmopoulos A., Bousias S., Fardis M.N.*; Design and Pre-test Assessment of 3-Storey Torsionally-Unbalanced RC Test Structure. Proceedings of fib Symposium: Concrete Structures in Seismic Regions, Athens, 2003

[16] *Mola E., Negro P.*; Full-Scale PsD Testing of the Torsionally Unbalanced SPEAR Structure in the As-Built and Retrofitted Configurations. Proceedings of SPEAR Workshop (M.N. Fardis and P. Negro, eds.), Ispra (IT), 2005; p.139-154

[17] *Kosmopoulos A., Fardis M.N.*; Seismic Testing of 3-Storey Full-Scale Torsionally Unbalanced RC Structure: Pre-test Predictions, Design and Analyses of Retrofitting. Proc. 5th Intern. PhD Symp. Civil Engineering, 2004; Delft, p.1115-1123

[18] *Kosmopoulos A., Bousias S., Fardis M.N.*; Seismic Rehabilitation of a Theater Facility according to Eurocode 8 using CFRPs. Proc. 8th Intern. Symposium on Fiber Reinforced Polymer Reinforcement for Concrete Structures (FRPRCS-8), 2007; Patras